Development of Analysis Techniques for dynamic magnetic resonance imaging

– Master Thesis –

to be awarded

Master of Science in Medical Photonics

submitted by

Aayush Nepal

May 15, 2024

Aayush Nepal
aayush.nepal@uni-jena.de
Student ID: 198683
Address:
Schützenggase 2
99423 Weimar

Supervisor

1st: Prof. Dr. rer. nat. med. habil. Jürgen Reichenbach
2nd: Dr. rer. nat. Martin Krämer

Friedrich-Schiller-Universität Jena
Medizinischen Fakultät
Institut für Diagnostische und Interventionelle Radiologie
Philosophenweg 3
07743 Jena

Abstract

Acknowledgements

Contents

List of Figures

List of Tables

List of Acronyms

FSU Jena Friedrich-Schiller-Universität Jena

1 Introduction

This thesis investigates the biomechanical analysis of the knee joint using high-resolution CINE MRI imaging, focusing on the dynamic interactions between the femur and tibia during flexion-extension cycles under various loading conditions. With advancements in MRI technology, detailed images of knee movements can be captured, which presents unique opportunities for extracting meaningful insights into invivo knee dynamics that can contribute to orthopedic research and clinical practice.

The primary challenge in utilizing these detailed images lies in the accurate segmentation of key anatomical structures. This segmentation is crucial, as it significantly influences the reliability of biomechanical measurements derived from the MRI data. Traditional manual segmentation methods, while straightforward, are time-consuming and prone to inconsistencies, especially when dealing with multiple frames across time. To address these issues, this thesis proposes the development of a semi-automated segmentation pipeline. This new methodology aims to streamline the segmentation process, reducing the time and effort involved while enhancing accuracy and consistency across sequential images.

Following the successful segmentation of the femur and tibia, the subsequent analysis involves quantifying two distinct biomechanical parameters: the angle between the long axes of the segments and the distance between specific anatomical landmarks on these bones. These measurements are calculated from single-slice 2D images in sagital view captured throughout the knee's motion cycle under both loaded and unloaded conditions. The purpose of this quantification is to explore potential differences in the kinematics of the knee joint under varying load and to provide an indirect assessment of joint space and functionality.

2 Fundamentals

2.1 The Knee Joint

The knee joint, a pivotal structure in the human body, plays an essential role in locomotion. Additionally, it functions to control the center of body mass and posture in the activities of daily living by facilitating a wide range of movements. As such, the knee's health and integrity are vital for overall quality of life, influencing

everything from basic mobility to participation in complex sports. A comprehensive survey across 15 European countries and Israel found that knee pain was the third most commonly reported type of chronic pain. This underscores the significant public health concern it represents (Breivik et al. 2006). Furthermore, arthritis/osteoarthritis (OA) was identified as the most common cause of this pain.

This situation has not improved over time. In Germany for instance, a recent retrospective study has found that the number of patients with OA is steadily rising (Obermüller et al. 2024). Knee-related issues are prevalent and impactful due to the inherent complexity of the knee joint itself. As a hub of various anatomical structures working in unison, the knee supports a range of movements and bears significant loads, making it susceptible to a variety of injuries and conditions. Understanding the anatomy of the knee is the first step in tackling this problem.

Anatomy and Function

The knee joint is the largest and the most superficial synovial joint in the body. (Dalley, Agur, and Moore 2023). It comprises three primary articulations:two femorotibial articulations (see Figure 1) and one femoropatellar articulation. These articulations, illustrated in Figure 1 and 2, are defined by their complexity and incongruence, features that are crucial for the joint's biomechanical performance.

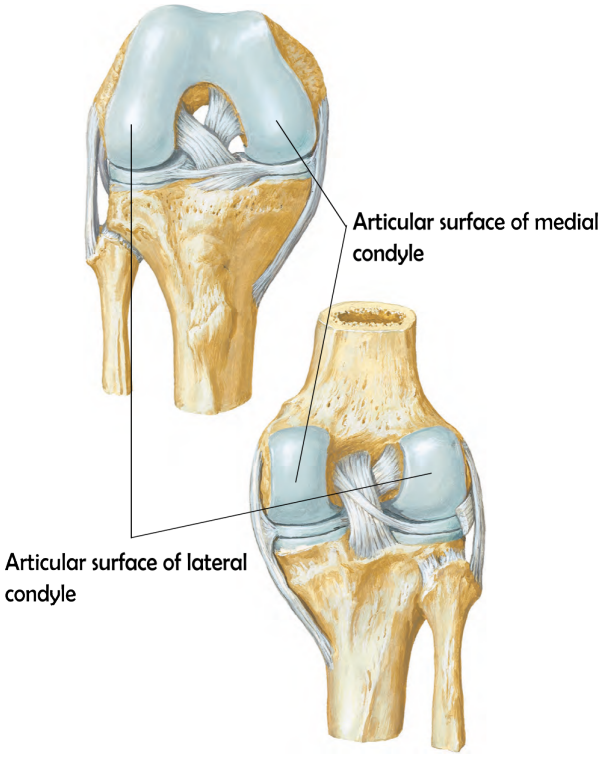

Figure 1: Anterior (flexed,top) and posterior (extended, bottom) view of the right knee with their articular surfaces labeled. [Edited] (Netter 2023, p.519)

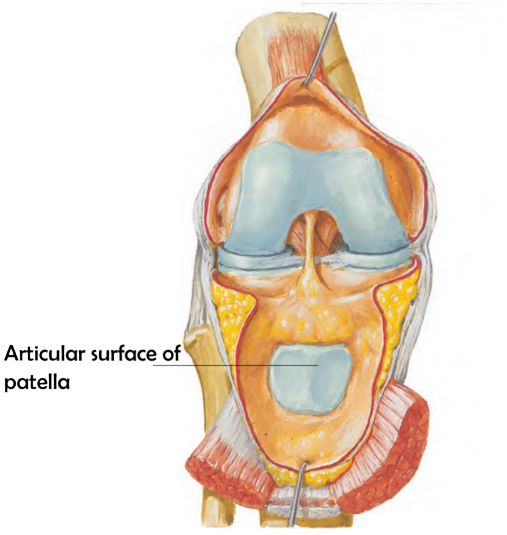

Figure 2: Right joint opened, knee slightly in flexion, with the patellar articulation labelled. [Edited] (Netter 2023, p.517)

This design allows the knee to manage a wide array of movements and bear significant loads. Figure 3 illustrates the knee's capacity for multidimensional movement,

highlighting the joint's sophisticated structural design that enables this versatility. However, this inherent design also renders the knee vulnerable to a range of forces (Standring and Gray 2021).

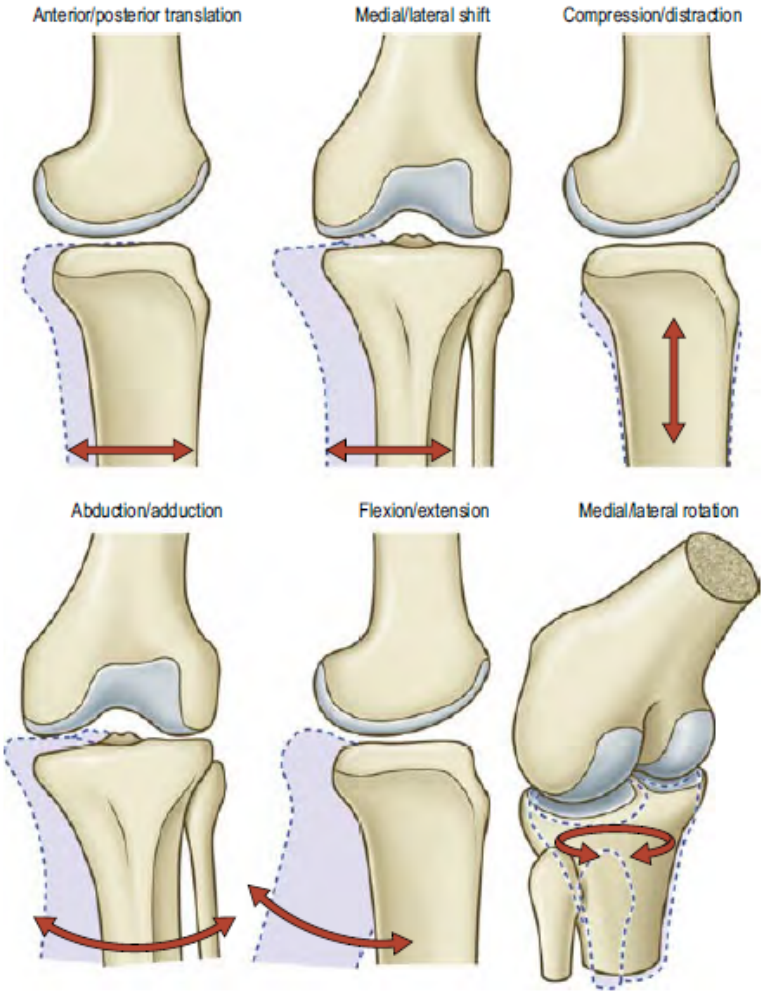

Figure 3: The knee joint motion in three dimensions, described using six independent variables (degrees of freedom) (Standring and Gray 2021, p. 1412).

Such mechanical forces, influenced by activities and body mass index (BMI), are significant causes of OA and represent one of the most modifiable risk factors (Heidari 2011). Furthermore, abnormal joint loading is considered a key mechanical driver of osteochondral changes thought to contribute to the initiation and progression of knee OA (Coburn et al. 2023).

The relationship between biomechanical stresses and knee health highlights the need for diagnostic tools that fulfill two key criteria: they must capture the knee's dynamic

behavior during motion and assess the joint under varying loads. Dynamic magnetic resonance imaging (MRI) excels in meeting these requirements as one of the most advanced imaging modalities.

2.2 Dynamic MRI

In a broad sense, dynamic MRI is an umbrella term encompassing various MRI techniques designed to capture and visualize physiological processes and motion over time. The dynamic aspect of MRI is crucial for studying systems or structures involving inherent motion, such as blood flow, tissue perfusion, or cardiac activity. For the purposes of this project, the focus of "dynamic MRI" narrows down to capturing the bulk movement of the knee joint undergoing active flexion extension cycles inside the scanner. Compared to traditional static MRI scans, which are highly susceptible to motion artifacts compared to other imaging modalities (Zaitsev, Maclaren, and Herbst 2015), dynamic MRI techniques not only accommodates motion, but can even leverage it to offer comprehensive insights into the functional and biomechanical properties of the concerned structures. Among these techniques, CINE imaging, particularly renowned in cardiac MRI, is considered the gold standard for evaluating cardiac function (Menchón-Lara et al. 2019). Its high regard in cardiac MRI demonstrates the method's precision and adaptability—traits that are leveraged in knee imaging.

2.2.1 CINE imaging

CINE, derived from 'cinematography,' refers to creating a movie-like sequence of images. In the context of dynamic knee MRI, this technique can be used to reconstruct a "movie" of a single flexion-extension cylce. This visualization is achieved by aggregating multiple partial datasets acquired over various cycles. The knee's movement cycle is segmented into distinct stages, each corresponding to a specific angle of flexion or extension. For each stage, k-space — the Fourier transform space from which MR images are reconstructed — is incrementally sampled. This data is gathered across multiple repetitions of the movement cycle, ensuring comprehensive coverage of k-space and thus, high-resolution imaging of each movement phase.This technique works robustly only if the movement cycles of the knee during imaging are sufficiently similar to each other (Curtis and Cheng 2022). Achieving this consistency in dynamic MRI of the knee, which naturally involves significant movement

variations, requires precise synchronization of the imaging process with the knee's motion cycle.

2.2.2 Gating

This synchronization, known as gating, aligns image acquisition with specific, repeatable points in the knee's movement cycle. By ensuring each captured image corresponds accurately to a consistent phase of motion, it minimizes the discrepancies that can arise from cycle-to-cycle variations, enhancing the reliability of bio-mechanical analyses. Retrospective gating, one of the two main types alongside prospective gating, provides consistent image quality. This makes it a suitable choice for applications like CINE imaging (Edelman 2005, p. 102). In retrospective gating, the data is acquired continuously throughout the motion cycle. The data is then reordered post-acquisition into a coherent sequence that shows the knee at different positions along the motion cycle. This necessitates external information that captures the precise moment and position of the knee throughout its range of movement beyond just the raw data acquired during the MRI scan. A previously reported novel knee loading device is employed to address this, which comes with an optical sensor attachment that provides this vital information. This sensor provides information that includes the exact timing and degree of knee flexion and extension, which is essential for accurately synchronizing the imaging frames with specific phases of the knee's motion cycle (Brisson et al. 2022).

2.2.3 Knee loading device

The MR-compatible knee loading device employed in this study is illustrated in Figure 5. This device allowed for a range of motion of approximately 25 to 45 degrees (subject-dependent), enabling subjects to perform knee flexion and extension cycles under both loaded and unloaded conditions. For loading, the device was equipped with compartments for weight plates and sandbags, providing a physiological load of 10 to 12 kilograms. These weights are positioned at the distal end of the device, directly influencing the mechanics of knee extension. As the subject extends the knee, they must overcome not only the natural resistance of their body weight but also the additional external load imposed by these weights. Central to this device's functionality is an optical fiber position sensor (MR338-Y10C10, Micronor, 155 Camarillo, CA, USA), which precisely measures the absolute angle from 0° to

360° with a resolution of 0.025°(Rickenbach 2013). This measurement capability is critical for synchronizing the knee's movement with MRI data reconstruction.

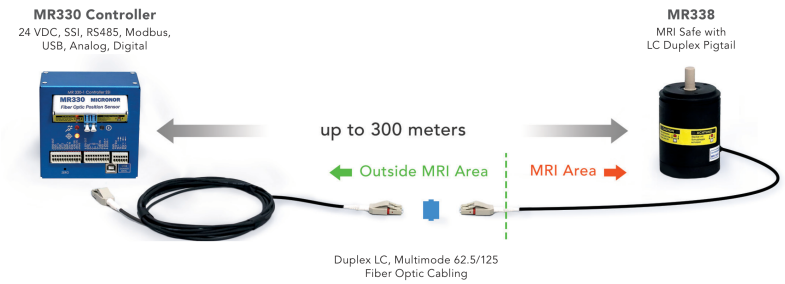

Figure 4: The MR330 controller (left) and MR338 optical fiber position sensor system (right), showcasing the connection from the controller to the sensor via duplex LC multimode fiber optic cabling.

As shown in Figure 4 , the MR330 controller interfaces with the MRI-safe MR338 position sensor to facilitate precise measurement within the MRI environment, accommodating up to 300 meters of fiber optic cabling. The controller is connected to a acquisition computer placed outside the scanner while the sensor is attached to the device within. To enhance signal acquisition and the clarity of imaging, two flexible coils (cite the coils here, perhaps also show a picture) were positioned at key anatomical locations: one at the distal femur and another at the proximal tibia, as specified in the MRI protocol.

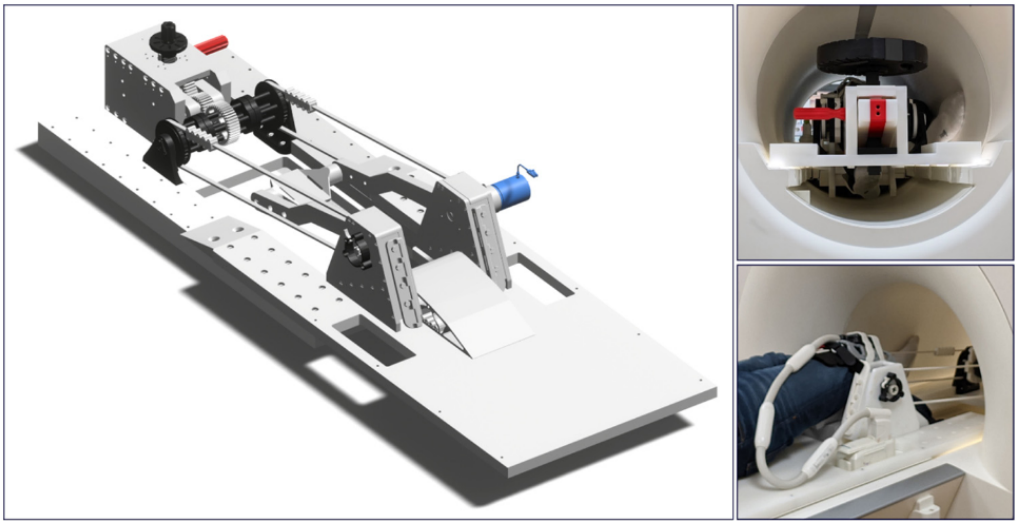

Figure 5: A 3D rendering of the knee motion/loading device (left) and two photographs of the device in a Siemens Magnetom Prisma Fit MRI scanner (right). The top right image (rear view) demonstrates how the distal part of the device sits atop the rails within the scanner bore, which are normally used to guide and support the patient table. The bottom right image (front, oblique view) demonstrates an individual positioned in the device with a flexible coil around the index knee, the thigh secured between the proximal pillow blocks and the ankle fastened to the leg support, as well as the coil plug setup (Brisson et al. 2022).

To further enhance the quality and precision of our imaging, and to maximize the potential for precise image reconstruction, a previously reported radial golden-angle gradient-echo FLASH sequence was used, which is more robust against motion artifacts than Cartesian sequences (Aleksiev et al. 2022). The following sections will detail the key components of this technique — radial golden-angle acquisition and the gradient-echo FLASH sequence.

2.2.4 Radial golden-angle acquisition

As the name suggests, radial golden-angle acquisition specifically modifies how k-space is sampled. Unlike traditional static MRI, which typically employs Cartesian sampling, this method utilizes radial sampling. Here, the data points are collected along radial lines spreading out from the center of k-space, resembling spokes on a wheel. Figure 6 depicts a generic radial sampling scheme. The separation between any two adjacent circles defines the separation Δk_r in the radial sampling direction, whereas, the angular separation between any two successive angular lines in k-space

(such as between the two example lines shown in the figure) defines $\Delta\theta$. The two quantities Δk_r and $\Delta\theta$ are constrained by the Nyquist sampling criterion. (Brown et al. 2014)

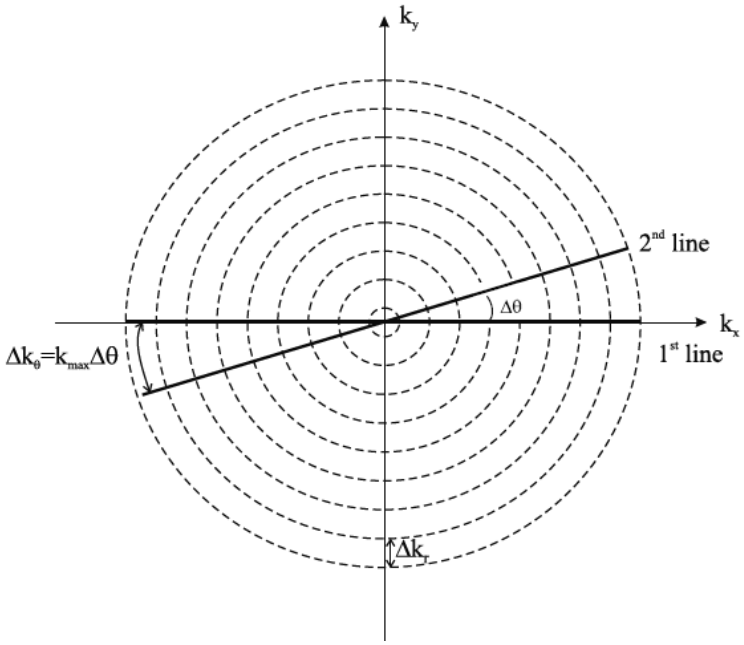

Figure 6: Generic radial k-space sampling (Brown et al. 2014, p.306)

The 'golden-angle' strategy, which we employ, optimizes this approach by spacing the radial lines at an angle of approximately 111.25 degrees. This specific angle helps in evenly covering the k-space without overlapping, ensuring that each new image frame provides unique information, thus enhancing image quality and temporal resolution.

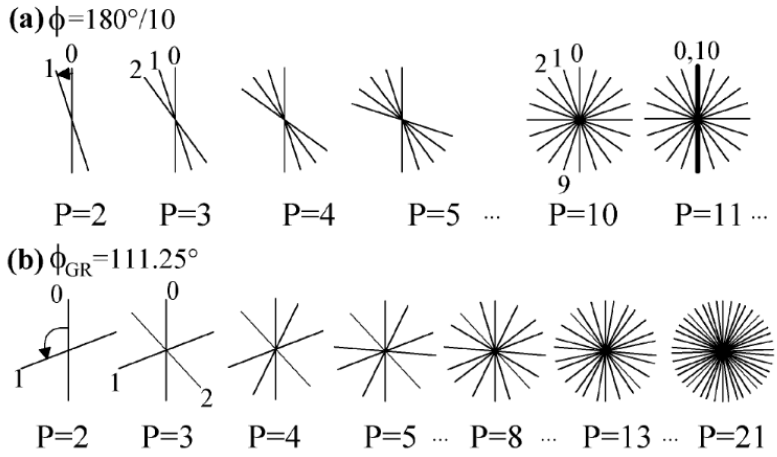

Figure 7: Radial k-space sampling strategies. (a) Fixed angular increment, showing potential for uneven k-space coverage. (b) Golden-angle sampling, ensuring uniform distribution across k-space (Winkelmann et al. 2007).

Figure 7 provides a visual comparison between traditional fixed increment and the golden-angle methods in k-space sampling. It highlights how each approach affects the distribution of sampling lines across k-space. In the figure, part (a) shows radial sampling using a fixed angular increment. This traditional method can lead to gaps or overlaps in data collection, depending on the number of radial profiles used. Part (b) demonstrates the golden-angle method, where each new radial line is placed at an increment of approximately 111.25 degrees. This approach allows for a more uniform distribution of sampling lines across the k-space, enhancing image quality by preventing gaps and reducing redundancy in data collection. Figure 8 shows the k-space of a specific frame during the knee flexion cycle and the corresponding reconstructed MRI image.

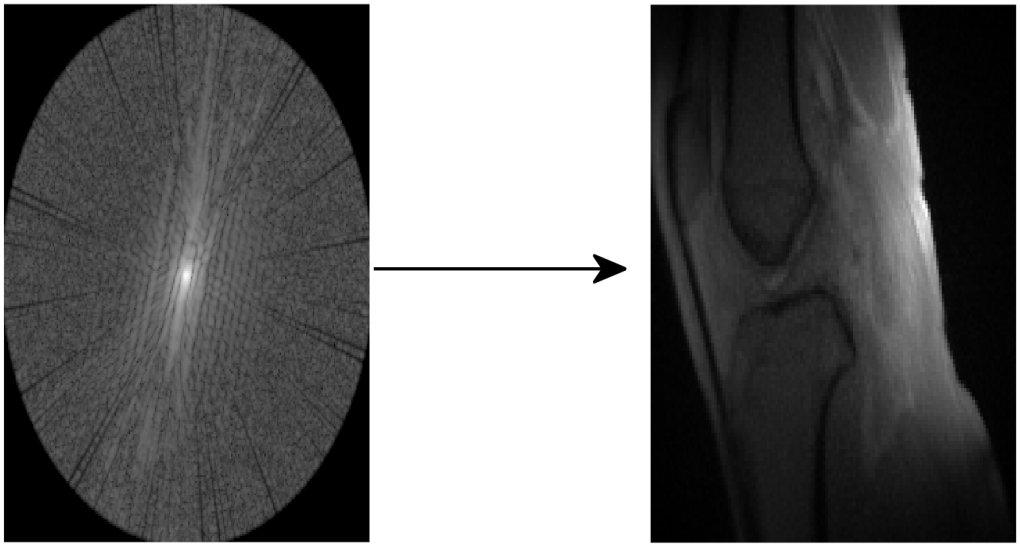

Figure 8: **Example of k-space and reconstructed image**. Left: K-space data from a specific angle during the knee flexion cycle. Right: Corresponding reconstructed MRI image, illustrating the detailed visualization achievable through golden-angle sampling.

2.2.5 Gradient Echo FLASH sequence

Gradient echo (GRE) imaging sequences are prime candidates for dynamic MRI because it is a fast scanning process. There are two major factors that contribute to its speed. First, unlike the spin echo, we do not need to wait for a long time for the longitudinal magnetization component M_z to sufficiently recover for another repetition. This is because in a GRE sequence, a smaller flip angle can be used. Secondly, we do not need to wait for the spins to refocus after the application of a 180^o rf pulse, because there is no such pulse applied. Instead, the refocusing is done here by using magnetic field gradients of opposite polarity. The scheme of GRE sequence is depicted in Figure 9. The notation is as follows: α^o: flip angle (less than 90^o), RF: radio frequency pulse, SS: slice selecting gradient, PE: phase encoding, FE: frequency encoding, TE: echo time and TR: repetition time. Note that in the frequency encoding direction, a negative dephasing lobe is followed by a positive gradient that brings the spins back into phase to generate the signal.

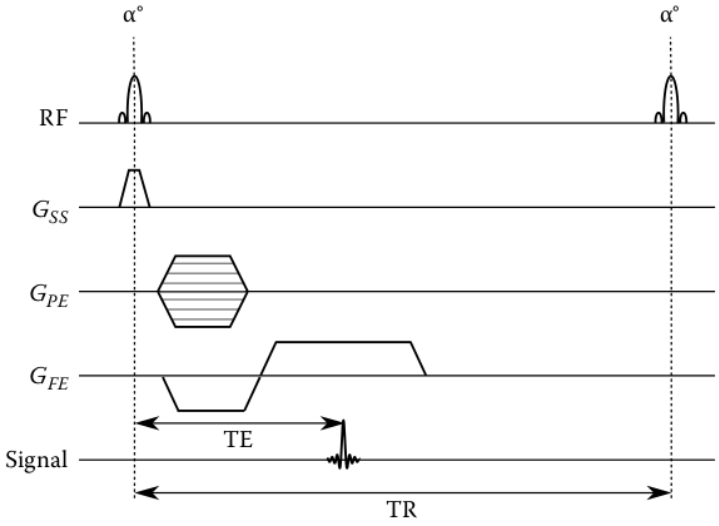

Figure 9: Simplified diagram of the GRE sequence that depicts the refocusing gradient applied in the frequency encoding direction (Berry and Bulpitt 2009, p.233).

After a series of rf pulses are applied, we reach a condition in gradient echo sequences called the **steady state.** In this state, the magnitude of the longitudinal magnetization component M_z is the same at the end of every TR. Similarly, we can also have a residual transverse magnetization M_{xy} at the start of every repetition cycle. If we deliberately dephase this residual transverse magnetization, the sequence is described as incoherent or spoiled gradient echo sequences.

FLASH is a type of spoiled GRE. It is a naming scheme that spells Fast Low-Angle Shot. (Haase et al. 1986) The introduction of the FLASH technique in the 1980s, known for its rapid acquisition capabilities, marked a significant advancement in MRI technology. It allowed for clearer imaging of dynamic processes and reduced artifacts associated with movement. The original paper on FLASH highlights the technique's potential for "recording NMR movies" to visualize physiological changes, a capability now fully integrated into contemporary MRI practices.

3 Methodology

3.1 Data Collection Methods

3.1.1 Procedure Details

Dynamic MRI scans were conducted on five healthy individuals, two females and three males, ranging in age from 28 to 39 years and weighing between 55 to 90 kilograms, utilizing a 3 T Siemens Prisma fit scanner. These volunteers were free from any known musculoskeletal disorders and provided their written consent, adhering to the ethical standards approved by the institutional review board. For all of these subjects, the left leg was scanned. In total, 7 unique datasets were acquired for analysis with two subjects measured twice on separate days to check for protocol stability.

Once the subject was positioned supine in the scanner, the thigh was secured on a wedge positioner, and the lower leg was attached to an ankle rest, just above the malleoli, using Velcro straps to minimize lateral movement. The knee to be examined is aligned with the device's axis of rotation, while the other leg rests alongside the MRI scanner's bore. Knee motion is guided by a belt and sprocket assembly running alongside the lower leg, connected to a gearbox activated by the leg support as the participant flexes and extends the knee. Once the subject was positioned at the scanner's isocenter, their leg naturally assumed a flexed posture due to the design of the device. In this configuration, the leg is cradled by the device arm which is positioned below the level of the knee, ensuring that the leg remains flexed without the volunteer exerting any force.

The volunteer engaged in a controlled exercise, following a metronome set at 60 beats per minute. This pace dictates a four-beat flexion to extension cycle, with the leg being flexed at the first beat and fully extended by the fourth. This equals to 8 beats per cycle, or 7.5 cycles every minute. Initially conducted under a loaded condition with weights added to the distal end of the device, the process is repeated without the added resistance to compare both states. The scan duration is around two and a half minutes, amounting to 20 full flexion-extension-flexion cycles.

3.1.2 Sequence Parameters and Reconstruction

Table 3.1.2, lists the MRI sequence parameters along with their respective units.

Table 1: MRI Sequence Parameters

Sequence Parameters	Values
Dimensions of raw data	(352, 276, 16, 100)
Acquisition Duration	160 [s]
Dwell Time	0.0024 [ms]
Echo Time	2.51 [ms]
Field Strength	2.89362 [T]
Flip Angle	8.0 [degrees]
Field of View (FOV)	192.0 x 192.0 x 3.0 [mm]
Frequency	123.25 [MHz]
Inversion Time	150000 [ms]
Matrix Size	176 x 176 x 1
Repetition Time	5.8 [ms]

In this study, the k-space data was acquired using 16 receive channels, each recording data simultaneously but with a unique spatial sensitivity profile. With 276 spokes used to sample a k-space dataset and a repetition time (TR) of 5.8 milliseconds per spoke, it takes approximately 1.6 seconds to acquire one k-space data. Over the course of the experiment, 100 such k-space datasets are acquired, equaling 100 repetitions as noted. The total scan duration extends just over two and a half minutes, a time frame reported by the subjects as being manageable, regardless of whether the scan was conducted under loaded or unloaded conditions.

Each k-space dataset contained data across a range of knee angles because of the continuous leg movement set to the metronome beat. This means, assuming the subjects perform perfectly in time of 60 beats per minute where we have 4 beats for flexion to extension, each k-space covers 0.4 times the range of motion. For example, a subject with a range of motion of 40^o, each k-space dataset contains data across 16^o. Therefore, with multiple repetitions, data across the full range of motion could be adequately acquired.

To illustrate the principle of radial k-space sampling, Figure X presents a simplified model, which includes only a few spokes and sampling points for visual purposes. In practice, as given in table 3.1.2, we have 352 points per spoke, and 276 spokes in total per k-space.

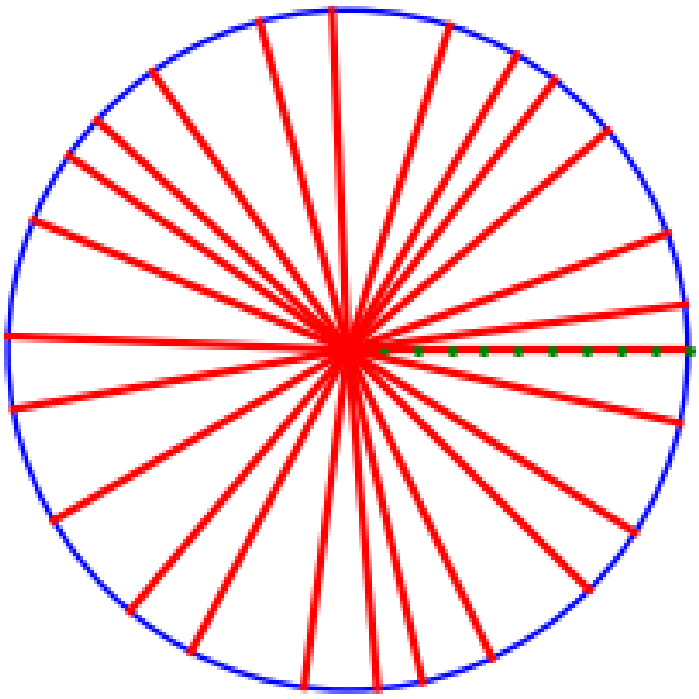

Figure 10: This illustration depicts a radial sampling pattern with 25 red spokes, using the golden angle for spacing. Only one spoke is detailed, showing 10 green points to represent sampling positions.

Reconstruction

The MRI raw data, with dimensions of (352, 276, 16, 100), was processed using a reconstruction script to generate the final image dataset. First, the binary data from the optical sensor was loaded, and the physical angle information was grouped according to each repetition cycle. This was done by detecting significant changes in the trigger signal, which was obtained from the sensor data too. This grouping resulted in 100 groups, each containing the physical angle information for a specific repetition. For each repetition, spokes in k-space were assigned to their corresponding physical angles. An angle increment of 2 degrees was chosen, which led to a collection of spokes corresponding to each 2-degree range. This approach was applied to all repetitions, allowing spokes to be mapped to physical angles across the full range of motion.

Subsequently, reconstruction was performed on each group of spokes. Depending on the specific angle range, the number of spokes assigned varied between 300 and

1000. Additionally, the direction of leg movement—either from flexion to extension or vice versa—was determined by calculating the slope of the angle information. Images were then reconstructed separately for each direction, depending on whether the leg was moving upward or downward. This distinction is crucial because leg biomechanics vary significantly depending on whether the movement is working with or against gravity.

The use of rielsing toolbox

The actual image reconstruction was done by using the Riesling reconstruction toolbox (Wood and contributors 2020). This toolbox offers a range of advanced algorithms tailored for non-Cartesian MRI reconstruction. In this study, an Alternating Direction Method of Multipliers (ADMM) approach was employed, incorporating Total Generalized Variation (TGV) regularization.

ADMM is an iterative optimization algorithm that breaks down complex problems into smaller subproblems to solve them efficiently. It ensures accurate reconstruction by maintaining a balance between the primal (actual solution) and dual (approximate solution) residuals. This balance is particularly important for non-Cartesian MRI reconstruction, given the unique geometry of the data. ADMM allows different regularization techniques, like TGV, to be applied simultaneously during reconstruction.(Boyd et al. 2011)

TGV is an advanced regularization method that reduces noise while promoting smoothness in the reconstructed images. Unlike basic Total Variation (TV) regularization, TGV allows for piecewise smooth transitions between different regions, making it better suited for images with varied structures. In this study, a regularization strength of 5e-2 was chosen empirically, striking a balance between noise suppression and edge detection.

The final reconstructed images were affected by the chosen reconstruction parameters, including the zero-filling factor and the field of view (FoV) trimming factor. The use of TGV regularization and the ADMM algorithm influenced the resulting image resolution, providing images with a consistent size suitable for downstream analysis. Each image frame was reconstructed with dimensions of (528, 528) and the number of frames were subject dependent.

3.2 Data Analysis

All the analysis and data visualization were done using the python programming language (v3.11.5). Several distinct steps were performed to semi-automate the segmentation of tibia and femur. This involves first finding one boundary edge each for the bones, and then tracking them across the full flexion-extension cycle by computing their respective transformation matrices.

3.2.1 Segmentation

The semi-auto segmentation process is achieved in five distinct steps as described below:

Step 1: Edge Detection

The Canny filter (Canny 1986), as implemented in the scikit-image's feature library (v0.21.0), was employed to apply an edge filter to the images. The Canny edge detection algorithm operates in several key steps to identify edges with high accuracy in images. Initially, the image is smoothed using a Gaussian filter to reduce noise and potential false edge detections. Following this, the algorithm calculates the gradient intensity and direction at each pixel, which helps in identifying the edges' boundaries.

Subsequently, the algorithm applies double thresholding, which involves two thresholds: a low and a high. This creates three categories of pixels: strong, weak, and non-edges. Pixels with intensities above the high threshold are marked as strong edge pixels, while those below the low threshold are considered to be non-edges. Pixels between these two thresholds are marked as weak edge pixels. Weak edge pixels are potentially converted into strong edges through a process known as hysteresis, where only those weak edges that are connected to strong edges are confirmed as true edges. In this context, hysteresis refers to the algorithm's reliance on the connectivity history of pixels to decide their edge status, ensuring that only meaningful, connected edges are preserved. This step is crucial for ensuring the continuity and completeness of detected edges.

To optimize the edge detection specifically to capture the desired edges of the tibia and femur, the different parameters like the standard deviation of gaussian blur (sigma) and the thresholds were tested in different combinations. The optimal results were achieved with a low threshold between 0 to 5 and a high threshold between

6 to 10. The sigma value was set at 2. Figure 11 displays the output of with these parameters.

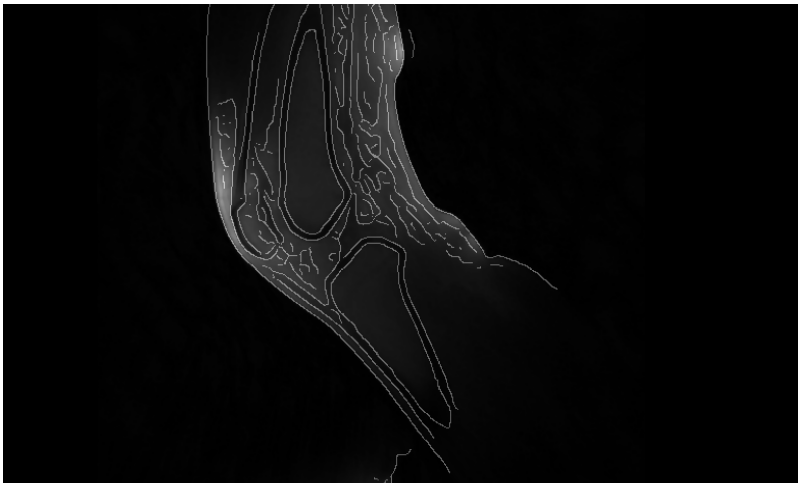

Figure 11: Output of the Canny edge detection algorithm applied to one of the frames, showing the detected edges of the tibia and femur bones overlayed on top of the original image for visual comparision.

Subsequently, the scikit-image's morphology library was utilized to remove small elements from the binary image. The image was then skeletonized to a one-pixel width, retaining only long and consistent edges. It should be pointed out that the final edge does not necesarrily need to span the full boundary of the interior edge of the cortical bone; even partial edges were successfully used for this purpose.

Step 2: Labelling

For the final selection of the desired edges, a labeling algorithm ('ndimage.label') from SciPy, an open-source Python library designed for scientific computing (version 1.11.3), was utilized. The purpose of employing this labeling algorithm is to effectively isolate specific structural features, such as distinguishing the interior cortical bone from the exterior, by assigning unique labels to separate closely situated edges detected in the image. This algorithm applies the principle of connected-component labeling, a method used in computer vision to detect connected regions in binary digital images. Connected-component labeling algorithm scans an image and groups its pixels into components based on pixel connectivity, meaning that all pixels in a connected component share similar pixel values and are adjacent to each other.

The labeling process treats any non-zero values in the input array as part of potential edges and zero values as background. The connectivity of these components is

determined by a structuring element, which in this case was a fully connected 3x3 matrix:

$$\begin{bmatrix} 1 & 1 & 1 \\ 1 & 1 & 1 \\ 1 & 1 & 1 \end{bmatrix}$$

This matrix is crucial as it defines the connectivity rules used during the labeling. Each pixel is considered connected to its eight immediate neighbors (above, below, left, right, and diagonals), known as eight-way connectivity. This element was chosen by trial and error. Alternatives, such as a four-way connectivity matrix, were tested but gave different labels to the same edge across frames. By using the eight-way connectivity, the same edge maintains consistent labeling across all frames, simplifying the analysis and reducing the need for manual adjustments.

Figure 12 shows the output from the labelling algorithm, where each color represents a separate label.

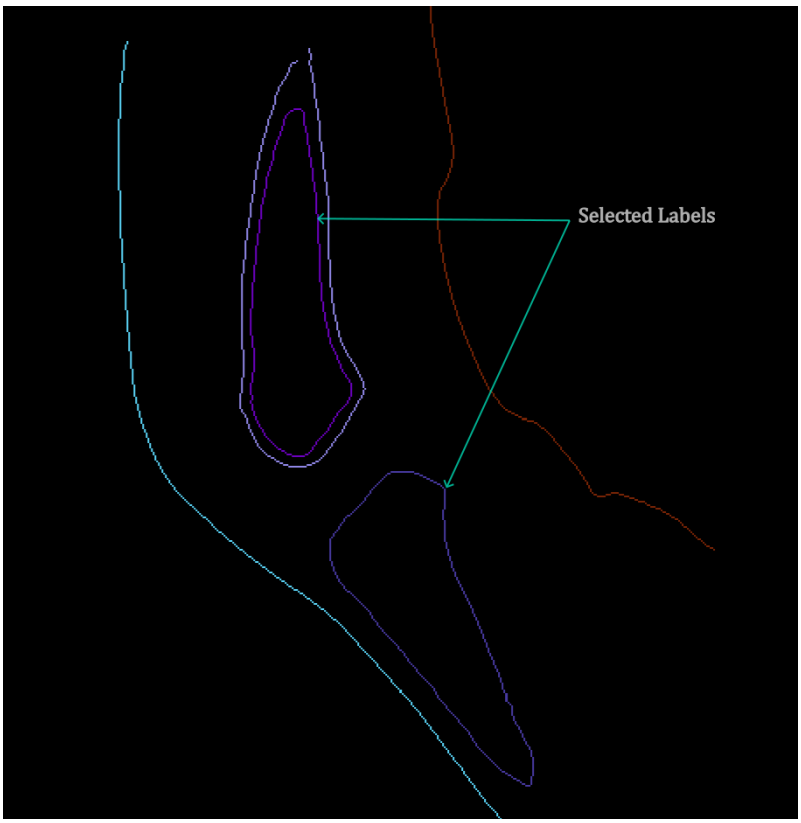

Figure 12: Output from the labeling algorithm with the representative edges for femur (top) and tibia(bottom) pointed out.

After choosing the appropriate labels, a binary image for each frame is obtained, where the foreground has the boundary for the interior edge of tibia and femur, and the background has intensity value of zero.

Step 3: Obtaining the set of reference points

Upon successfully isolating the binary edge images of the tibia and femur in Step 2, the subsequent step deals with establishing a set of reference points along each bone's edge in the first frame. This frame, captured when the knee is in a fully flexed position, serves as the reference frame for further analysis. This frame is chosen as the baseline (where transformations are initialized to zero) to facilitate the accurate calculation of rotation and translation matrices that describe the movement of the knee through subsequent frames. The purpose of establishing these reference points is twofold: to simplify the complex data set for efficient processing and to ensure a consistent basis for accurately calculating transformations between subsequent frames. This is essential, as direct use of the densely packed binary edge data would be computationally cumbersome and less precise for such transformations.

To begin, the points along the boundary were organised and sorted. This was done by first, defining a starting point, and then iteratively using a greedy nearest neighbor algorithm for sorting. The most distal point of the bone was taken as the initial seed. Various functions from the numeric python library 'Numpy' (v. 1.26.4) were employed for this task.

Once the points are sorted, the next step involves downsampling these points to a set of uniform equidistant reference points along the boundary of the binary edge. The necessity for this step arises from the inherent irregularity and density of the binary edge data. Directly sampling every n-th point from the sorted list would not suffice, as it could result in uneven spacing due to the variable distances between consecutive points in the original data.

This process begins by calculating the cumulative distances between each consecutive pair of points in the sorted list. Using these distances, a total path length is established. The desired interval between the new points is then determined by dividing this total path length by the number of intervals (number of desired points minus one).

Determining the optimal number of points—ranging between 50 to 80—was established through trial and error. Fewer than 50 points often compromised the accuracy of the edge overlap by failing to capture the essential contours of the bone. Con-

versely, exceeding 80 points did not significantly enhance the algorithm's accuracy but increased the code execution time slightly.

To achieve precise positioning of these points, cubic spline interpolation from SciPy's interpolate libary was used. This interpolation method is particularly effective for ensuring that the new points adhere closely to the original curve while maintaining equidistance. Figure 13 depicts this result.

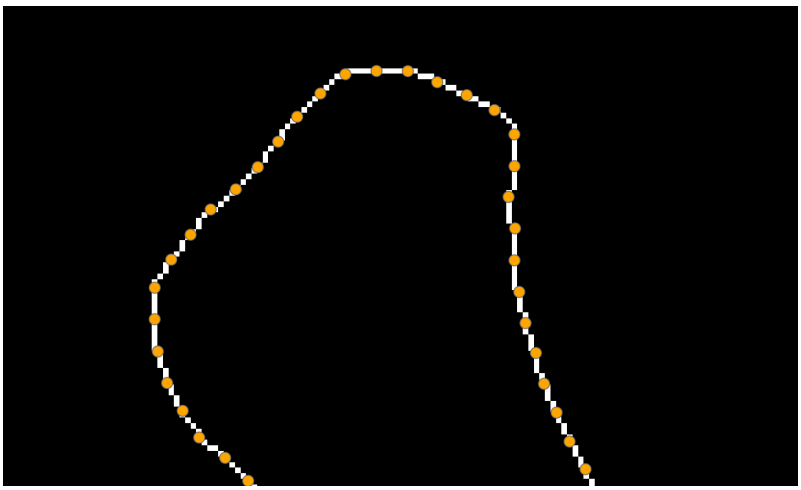

Figure 13: A zoomed in look at the equidistant sampled points (orange) along the boundary of the tibia edge (white).

Step 4: Transformation matrices computation

In this step, a set of transformation matrices is obtained, each containing the parameters that align a segment of the bone from one frame to the next. These transformations includes solely the translation in the sagittal plane and rotation about the transverse axis. This approach assumes that the bone does not undergo any deformation and that through-plane motion is negligible throughout the motion cycle.

Mathematically, the transformation of each point from one frame to the next can be expressed as

$$p^{'} = R(\phi)p + t \tag{1}$$

where:

- p is the coordinate of the point in its current frame
- $p^{'}$ is the coordinate of the point after transformation

- ϕ is the angle of rotation
- $R(\phi)$ is the rotation matrix, given by

$$R(\phi) = \begin{bmatrix} \cos\phi & -\sin\phi \\ \sin\phi & \cos\phi \end{bmatrix}$$

- t is the translation vector,

$$t = \begin{bmatrix} x \\ y \end{bmatrix}$$

- x and y are the translations in the Cartesian coordinate system.

As such, only three parameters, x, y, and ϕ need to be computed. To determine these parameters, a cost function is defined. This function, denoted as $C(x, y, \phi)$, quantifies the alignment error by calculating the 'cost' of deviations for any given set of transformation parameters. The minimization of this cost identifies the combination of parameters that achieves the best alignment or overlap of the transformed frame with the reference frame. A lower value of the cost function output indicates a closer match to the target frame, suggesting a superior alignment, whereas a higher value signifies a less accurate alignment. The cost function is defined in Equation 2:

$$C(x, y, \phi) = \sum_{p=1}^{N} \min_{q \in Q} \left(\sqrt{(x_q - x'_p)^2 + (y_q - y'_p)^2} \right) \tag{2}$$

where:

- (x_p, y_p) are the coordinates of points in the reference frame
- (x'_p, y'_p) are the coordinates of points after transformation:

$$x'_p = x + x_p \cos(\phi) - y_p \sin(\phi)$$
$$y'_p = y + x_p \sin(\phi) + y_p \cos(\phi)$$

- (x_q, y_q) are the coordinates of points in the target frame.
- N is the number of points in the reference frame, and Q represents all points in the target frame.

This cost function evaluates the alignment of transformed coordinates to target coordinates by calculating the sum of the shortest distances from each point in the transformed frame to the closest point in the target frame. Each (x'_p, y'_p) is the position of a point from the reference frame after being transformed by the parameters x, y, and ϕ. For each transformed point,the distance to every point (x_q, y_q) in the target frame is computed, the minimum of these distances is selected, and sum these minimum distances across all points is calculated. This sum forms the output of the cost function, which we seek to minimize.

The optimization of this cost function is performed using a nonlinear least squares approach, where the initial guess of [0,0,0] is provided. The optimization process uses the `fmin` function from SciPy's optimization module, which is configured to stop when the change in the cost function is below a small tolerance. Figure 14 provides a visual representation of the overlap of the reference points from the fully flexed initial position to the frame where the lower leg has been rotated by an angle of 12 degrees as reported by the rotary angle encoder.

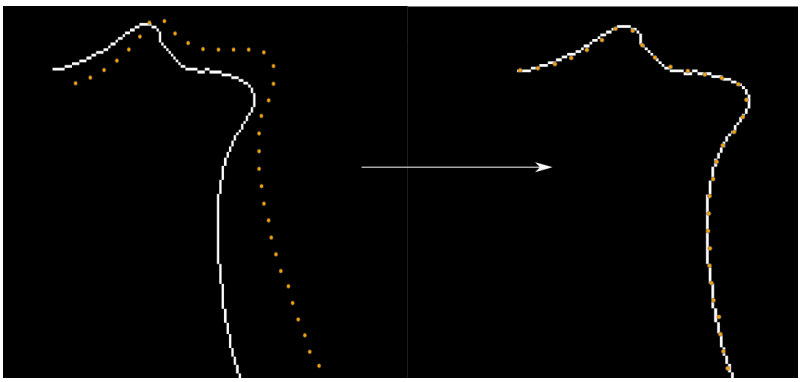

Figure 14: Left: The reference points in the first frame (orange) overlaid with the binary edge image of the target frame (white).Right: The reference points have been transformed by using the results from the optimization showing almost perfect overlap, illustrating the effective alignment achieved through the minimization of the cost function.

Step 5: Auto-Segmentation

With the transformation matrices obtained for the femur and the tibia, manual segmentation is performed on the first frame. An example is given in figure 15.

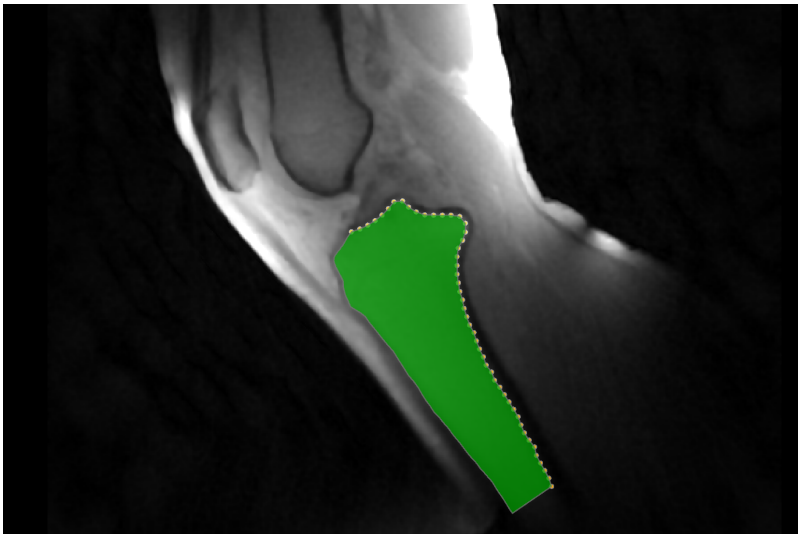

Figure 15: Manual segmentation is performed to complete the boundary of the tibia's interior edge shown in green, along with the reference points (orange).

Using the points from this segment, the transformation matrices are now applied once more using equation 1 to transform one frame to the next subsequently to complete the full segmentation across all the frames automatically.

3.2.2 Extraction of Biomechanical Parameters

After achieving automated segmentation of the tibia and femur across all frames, the next step involved extracting biomechanical parameters from the segmented regions. Two key metrics were considered for analysis to assess the relationship between these bones throughout the flexion-extension cycle captured in the 2D Cine images.

The first metric involved calculating the angle between the long axis of femur and tibia segments. This measurement provided insight into how the relative orientation of the two bones changes over time.

The second metric measured the distance between specific anatomical landmarks on both the femur and tibia. Tracking this distance across the frames offered an understanding of how the spatial relationship between these two bones evolved during the motion cycle.

Angle between the bones

To calculate the angle between the bones, the long axis of each bone segment was identified using a technique called Principal Component Analysis (PCA). The anal-

ysis was performed using the PCA implementation from the scikit-learn (v1.3.1) Python library, a module for machine learning built on top of SciPy.

PCA determines the direction of maximum variance in the data, which coincides with the longitudinal axis of the bone. PCA first uses the coordinates of the segmented binary mask as input. The centroid of the shape is calculated and subtracted from each data point, centering the data such that the mean of this transformed data is (0, 0).

Next, the covariance matrix (Cov) is computed, a square matrix that gives an indication of how the data varies along each dimension and how different dimensions vary together.

$$\text{Cov} = \begin{bmatrix} \text{Var}(X) & \text{Cov}(X,Y) \\ \text{Cov}(Y,X) & \text{Var}(Y) \end{bmatrix} \tag{3}$$

where:

- $\text{Var}(X)$ is the variance of X, given by:

$$\text{Var}(X) = \frac{1}{N-1}\sum_{k=1}^{N}(X_k - \bar{X})^2,$$

  where N is the number of points, X_k represents the k^{th} observation in the X dimension, and $\bar{X}$ is the mean value of all observations in the X dimension.

- $\text{Cov}(X,Y)$ is the covariance between dimensions X and Y, defined as:

$$\text{Cov}(X,Y) = \frac{1}{N-1}\sum_{k=1}^{N}(X_k - \bar{X})(Y_k - \bar{Y}),$$

  where Y_k represents the k^{th} observation in the Y dimension, and $\bar{Y}$ is the mean value of all observations in the Y dimension.

- $\text{Cov}(Y,X)$ is equivalent to $\text{Cov}(X,Y)$ because the covariance matrix is symmetric.

- $\text{Var}(Y)$ is the variance of Y, calculated similarly to $\text{Var}(X)$.

When this covariance matrix is applied to a vector, the matrix transforms the vector such that it aligns more closely with the direction of maximum variance in the

dataset. Therefore, by computing the matrix's eigenvectors and eigenvalues, the vectors representing the direction of maximum variance is identified. The first principal component refers to the eigenvector associated with the largest eigenvalue. In figure 16, the longitudinal axis of femur and tibia are shown.

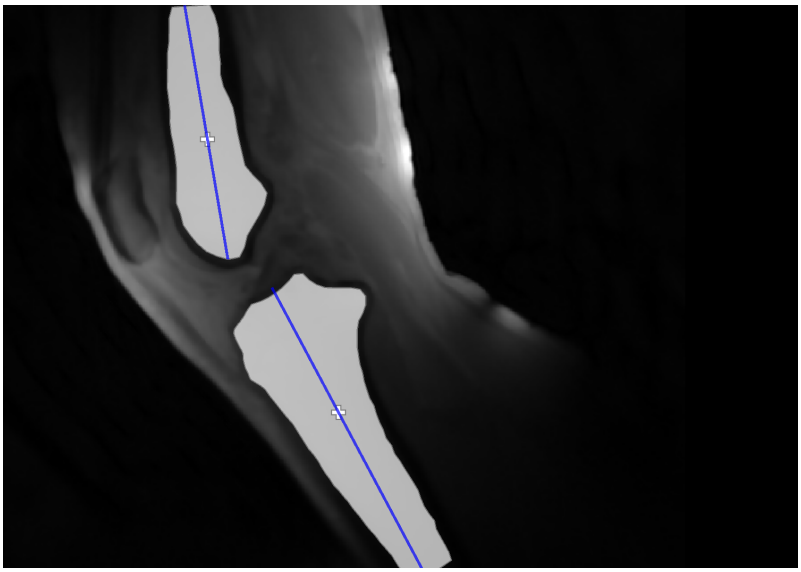

Figure 16: The long axis of the bones are identified by using the PCA (blue) along with the centroid (white cross) for each segment

The angles between the segments was calculated by using the dot product between unit vectors, as given in equation 4

$$\theta = \arccos(\mathbf{U}_{fem} \cdot \mathbf{U}_{tib}) \tag{4}$$

where, $\mathbf{U_{fem}}$ and $\mathbf{U_{tib}}$ are the unit vectors of the longitudinal axes for the femur and tibia segments respectively.

Distance between the bones

To calculate a proxy for the distance between the bones, anatomical landmarks were identified for the bones. The most distal point on the femur segment was chosen for the femur and a point on the proximal tibia for the tibia as shown in figure 17.

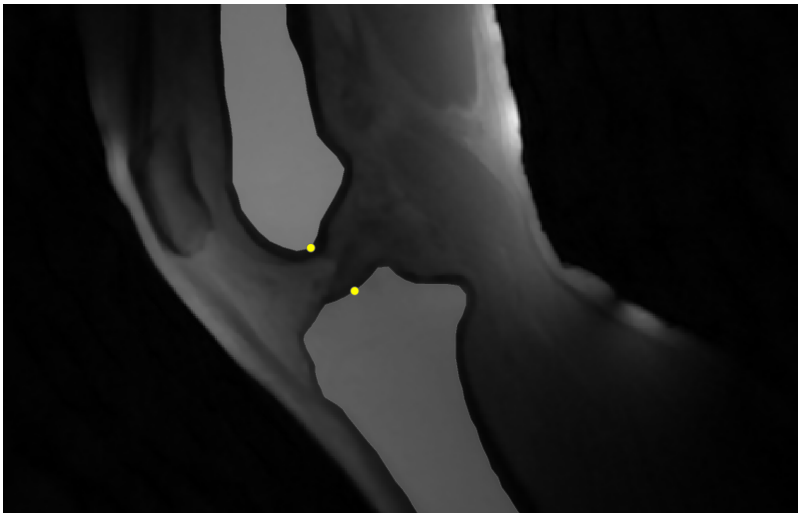

Figure 17: Points based on anatomical landmarks are shown in yellow.

The euclidean distance between these two points was measured across time by using equation blank:

$$d = \sqrt{(y_2 - y_1)^2 + (x_2 - x_1)^2} \tag{5}$$

4 Results

4.1 Accuracy of edge tracking and segmentation

To evaluate the accuracy of edge tracking achieved through cost function minimization, the deviation of overlap between points on the transformed frame and the target frame was measured. The cost function output, which indicates the overlap accuracy, calculates the minimum distance from each point on the transformed frame to the points on the target frame and sums these minimum distances for all points in the transformed frame.

The mean alignment error per point was derived by dividing the cost function output by the total number of points in the transformed frame. This value was calculated for all frames, and the average of these values was taken for each dataset.

The bar chart in Figure 18 presents this result:

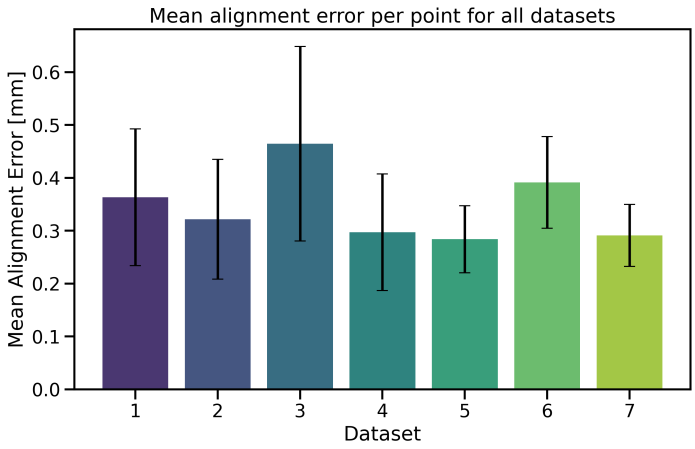

Figure 18: Mean alignment error per point across all frames for each dataset in the unloaded condition.

The result of the segmentation for one of the datasets is given in figure 19.

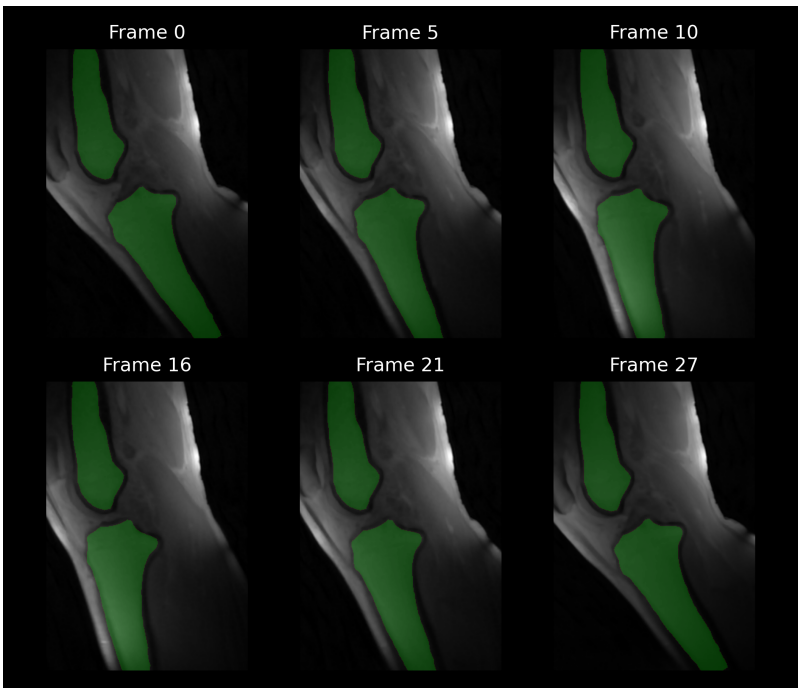

Figure 19: A mosaic showing the segmented tibia and femur shapes(green) where each tile is a particular time point. The leg is fully flexed at Frame 0

4.2 Results of biomechanical parameter extraction

To ensure consistent comparisons, the number of frames reconstructed, which represents the time axis, is grouped into 'bins'. This grouping allows all datasets to span the same bins, enabling the averaging and plotting of values within these bins. The axis is defined by the percentage of flexion at a given time point. For all datasets, the data begins at the maximally flexed position, progresses to full extension, and then returns to the maximally flexed position. In this context, maximal flexion is defined as -100%, full extension as 0%, and the return to maximal flexion as 100%.

Angle calculation

Figure blank displays the result of calculating the angle between the long axes of bone segments across the flexion-extension cycle.

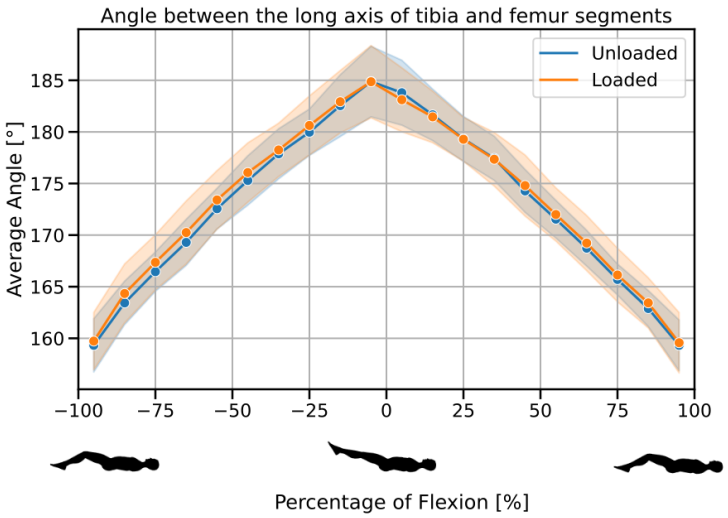

Figure 20: Plot of angle between long axes of bone segments between tibia and femur versus the flexion percentage.

Distance calculation

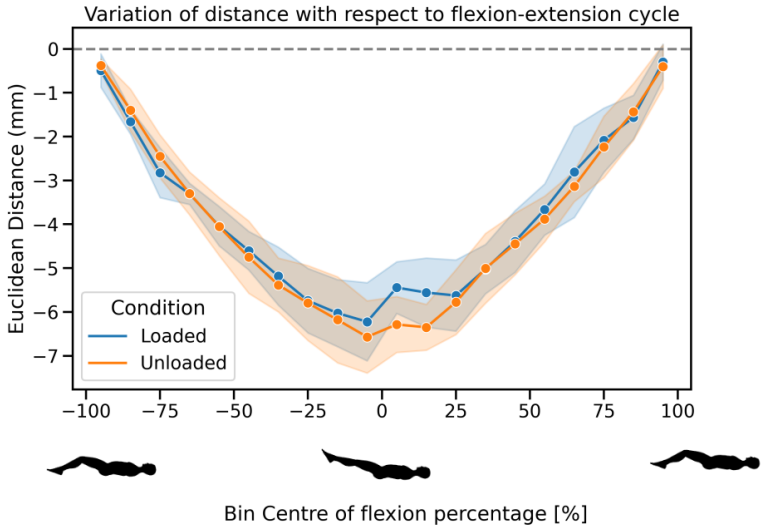

Figure 21: Plot showing the variation of euclidean distance between two points with respect to different time points in the motion cycle. The shaded region represents one standard deviation uncertainty.

Bin (0.0, 10.0]: T-statistic = 2.581347448142401, P-value = 0.021752348033689917
Bin (10.0, 20.0]: T-statistic = 2.651870913157143, P-value = 0.015303907958726073

5 Discussion

5.1 Edge tracking and segmentation

The accuracy of segmentation in this study is fundamentally tied to the precision of edge tracking, as the segment boundary is defined by the detected edges. Thus, the fidelity of the segmentation process is directly influenced by the accuracy of edge detection. The edge tracking accuracy, in turn, hinges on two key factors: the assumption of single-plane motion and the quality of the image data.

Firstly, the assumption of single-plane motion with rotation and translation is crucial. If there is any through-plane motion, the resulting transformations will be inaccurate since the algorithm is designed to handle only rigid transformations within a single plane. Deviations from this assumption will inevitably lead to errors in edge detection

Secondly, the quality of the cine MRI images plays a significant role. Inconsistent movements during the imaging process can cause blurring, which the reconstruction

algorithm cannot fully mitigate. Blurred images lead to less precise edge detection by the Canny algorithm, thereby affecting the accuracy of the segmentation.

The performance of the edge tracking algorithm is illustrated by the bar chart in Figure 18, which shows the mean alignment error per point across seven different datasets. The mean alignment errors range from approximately 0.3 mm to 0.5 mm, with datasets 2,4,5 and 7 demonstrating the smallest errors around 0.3 mm. In contrast, dataset 3 shows the highest mean alignment error, slightly lower than 0.5 mm, and also exhibits the largest variability, as indicated by the error bars. This variability suggests that the algorithm's performance might be less consistent for certain datasets.

Despite this, the overall accuracy of the edge tracking algorithm is notable. The observed mean alignment errors, even at their highest, are relatively small, with the largest mean error being around 0.5 mm.

To illustrate the reliability of the edge tracking algorithm, the results are compared with those of Rathnayaka et al. (2012), who quantified the accuracy of MRI-generated 3D models of long bones, reporting an average error of 0.23 mm (Rathnayaka et al. 2012). Although the mean alignment errors in this study are slightly higher, the methodology—measuring the mean alignment error by calculating the average point-to-point distance between corresponding points in the transformed and target frames—is conceptually similar. This comparison indicates that the precision of the algorithm is within a reasonable range, supporting its reliability for segmentation purposes.

6 Conclusion

References

Aleksiev, Martin et al. (Oct. 2022). "High-resolution CINE imaging of active guided knee motion using continuously acquired golden-angle radial MRI and rotary sensor information". In: *Magnetic Resonance Imaging* 92, pp. 161–168. ISSN: 0730725X. DOI: 10.1016/j.mri.2022.06.015. URL: https://linkinghub.elsevier.com/retrieve/pii/S0730725X22001096 (visited on 02/12/2024).

Berry, Elizabeth and Andrew J. Bulpitt (2009). *Fundamentals of MRI: an interactive learning approach*. eng. OCLC: 872673253. Boca Raton, Florida: CRC Press. ISBN: 978-1-58488-902-1.

Boyd, Stephen et al. (2011). "Distributed Optimization and Statistical Learning via the Alternating Direction Method of Multipliers". In: *Foundations and Trends® in Machine Learning* 3.1, pp. 1–122. ISSN: 1935-8237. DOI: 10.1561/2200000016. URL: http://dx.doi.org/10.1561/2200000016.

Breivik, Harald et al. (May 2006). "Survey of chronic pain in Europe: Prevalence, impact on daily life, and treatment". In: *European Journal of Pain* 10.4, pp. 287–287. ISSN: 1090-3801, 1532-2149. DOI: 10.1016/j.ejpain.2005.06.009. URL: https://onlinelibrary.wiley.com/doi/10.1016/j.ejpain.2005.06.009 (visited on 03/27/2024).

Brisson, Nicholas M. et al. (Nov. 2022). "A novel multipurpose device for guided knee motion and loading during dynamic magnetic resonance imaging". en. In: *Zeitschrift für Medizinische Physik* 32.4, pp. 500–513. ISSN: 09393889. DOI: 10.1016/j.zemedi.2021.12.002. URL: https://linkinghub.elsevier.com/retrieve/pii/S093938892100115X (visited on 02/12/2024).

Brown, Robert W. et al. (2014). *Magnetic resonance imaging: physical principles and sequence design*. Second edition. Hoboken, New Jersey: John Wiley & Sons, Inc. 944 pp. ISBN: 978-0-471-72085-0.

Canny, John (Nov. 1986). "A Computational Approach to Edge Detection". In: *IEEE Transactions on Pattern Analysis and Machine Intelligence* PAMI-8.6, pp. 679–698. ISSN: 0162-8828. DOI: 10.1109/TPAMI.1986.4767851. URL: https://ieeexplore.ieee.org/document/4767851 (visited on 02/18/2024).

Coburn, Sally L. et al. (July 14, 2023). "Immediate and Delayed Effects of Joint Loading Activities on Knee and Hip Cartilage: A Systematic Review and Meta-analysis". In: *Sports Medicine - Open* 9.1, p. 56. ISSN: 2198-9761. DOI: 10.1186/s40798-023-00602-7. URL: https://sportsmedicine-open.springeropen.com/articles/10.1186/s40798-023-00602-7 (visited on 04/07/2024).

Curtis, Aaron D. and Hai-Ling M. Cheng (Feb. 2022). "Primer and Historical Review on Rapid Cardiac ¡span style="font-variant:small-caps;"¿CINE MRI¡/span¿". en. In: *Journal of Magnetic Resonance Imaging* 55.2, pp. 373–388. ISSN: 1053-1807, 1522-2586. DOI: 10.1002/jmri.27436. URL: https://onlinelibrary.wiley.com/doi/10.1002/jmri.27436 (visited on 04/09/2024).

Dalley, Arthur F., A. M. R. Agur, and Keith L. Moore (2023). *Moore's clinically oriented anatomy*. Ninth edition. Philadelphia: Wolters Kluwer. 1 p. ISBN: 978-1-975154-08-0.

Edelman, Robert R., ed. (2005). *Clinical magnetic resonance imaging*. Philadelphia, Pa.: Saunders. ISBN: 978-0-7216-0306-3.

Haase, A et al. (Apr. 1986). "FLASH imaging. Rapid NMR imaging using low flip-angle pulses". en. In: *Journal of Magnetic Resonance (1969)* 67.2, pp. 258–266. ISSN: 00222364. DOI: 10.1016/0022-2364(86)90433-6. URL: https://linkinghub.elsevier.com/retrieve/pii/0022236486904336 (visited on 04/19/2024).

Heidari, Behzad (2011). "Knee osteoarthritis prevalence, risk factors, pathogenesis and features: Part I". In: *Caspian Journal of Internal Medicine* 2.2, pp. 205–212. ISSN: 2008-6164.

Menchón-Lara, Rosa-María et al. (Sept. 23, 2019). "Reconstruction techniques for cardiac cine MRI". In: *Insights into Imaging* 10.1, p. 100. ISSN: 1869-4101. DOI: 10.1186/s13244-019-0754-2.

Netter, Frank H. (2023). *Netter atlas of human anatomy: classic regional approach*. Eighth edition. Philadelphia, PA: Elsevier. ISBN: 978-0-323-68042-4.

Obermüller, Dominik et al. (Mar. 2024). "Epidemiology and treatment of pain associated with osteoarthritis of the knee in Germany: A retrospective health claims data analysis". In: *Osteoarthritis and Cartilage Open* 6.1, p. 100430. ISSN: 26659131. DOI: 10.1016/j.ocarto.2023.100430. URL: https://linkinghub.elsevier.com/retrieve/pii/S2665913123000973 (visited on 03/27/2024).

Rathnayaka, Kanchana et al. (Apr. 2012). "Quantification of the accuracy of MRI generated 3D models of long bones compared to CT generated 3D models". en. In: *Medical Engineering & Physics* 34.3, pp. 357–363. ISSN: 13504533. DOI: 10.1016/j.medengphy.2011.07.027. URL: https://linkinghub.elsevier.com/retrieve/pii/S1350453311001925 (visited on 05/15/2024).

Rickenbach, Robert (June 11, 2013). "Optical spectrum modulated position sensor having a controller with at least one fiber optic line". U.S. pat. 8461514B1. Indi-

vidual. URL: https://patents.google.com/patent/US8461514B1/en?oq=US-8461514-B1 (visited on 04/23/2024).

Standring, Susan and Henry Gray, eds. (2021). *Gray's anatomy: the anatomical basis of clinical practice*. Forty-second edition. OCLC: on1202943188. Amsterdam: Elsevier. 1588 pp. ISBN: 978-0-7020-7705-0.

Winkelmann, Stefanie et al. (Jan. 2007). "An Optimal Radial Profile Order Based on the Golden Ratio for Time-Resolved MRI". en. In: *IEEE Transactions on Medical Imaging* 26.1, pp. 68–76. ISSN: 0278-0062. DOI: 10.1109/TMI.2006.885337. URL: http://ieeexplore.ieee.org/document/4039540/ (visited on 04/18/2024).

Wood, Tobias C. and contributors (2020). *Riesling: A reconstruction toolbox optimized for 3D non-cartesian MR images*. Presented at ISMRM 2020. URL: https://github.com/spinicist/riesling.

Zaitsev, Maxim, Julian Maclaren, and Michael Herbst (Oct. 2015). "Motion artifacts in MRI: A complex problem with many partial solutions". eng. In: *Journal of magnetic resonance imaging: JMRI* 42.4, pp. 887–901. ISSN: 1522-2586. DOI: 10.1002/jmri.24850.

A Appendix

If needed for supplementary material, such as detailed description of data collection, tables, or figures.

Statutory Declaration:

I declare that I have developed and written the enclosed Master Thesis completely by myself, and have not used sources or means without declaration in the text. Any thoughts from others or literal quotations are clearly marked. The Master Thesis was not used in the same or in a similar version to achieve an academic grading or is being published elsewhere.

Place, Date

Signature